Submitted to ***Canadian Geotechnical Journal***

Neutral network-assisted generic predictive models of safety factor and yield acceleration for seismic slope stability and displacement assessments

Mao-Xin Wang[a], Y.F. Leung[a], Dian-Qing Li[b]

[a] Department of Civil and Environmental Engineering, The Hong Kong Polytechnic University, Hung Hom, Hong Kong SAR, China

[b] State Key Laboratory of Water Resources Engineering and Management, Institute of Engineering Risk and Disaster Prevention, Wuhan University, 299 Bayi Road, Wuhan, 430072, China

Correspondence to: Y.F. Leung (E-mail: andy.yf.leung@polyu.edu.hk)

Abstract

As two well-recognized approaches for seismic slope stability assessment, the pseudo-static analysis estimates the factor of safety (*FS*) and the Newmark-type analysis estimates permanent downslope-displacement based on input yield acceleration (k_y). However, *FS* and k_y are usually obtained from non-trivial slope stability calculations, which can become computationally demanding in probabilistic analyses or regional landslide mapping. This study presents neural network-assisted predictive models for (1) seismic or static *FS* and the category of failure mode; and (2) k_y and the thickness of failure mass. Extensive stability analyses of more than 741,000 and 123,000 slope configurations are conducted to compile datasets of *FS* and k_y, respectively. Performance evaluations indicate that the models produce physically reasonable prediction trends and have good generalization capability with correlation coefficient higher than 0.94 in blind tests. Compared to the existing infinite slope model and predictive tools, the new models achieve improved applicability and functionality, accounting for pore-water pressure, depth to hard stratum, and various failure modes. Both the spreadsheet and MATLAB files established in this study are provided to facilitate generic applications. Therefore, this work not only demonstrates the neural network capability, but also provides useful tools for practitioners, contributing to both the pseudo-static and Newmark-type approaches.

Keywords: Pseudo-static slope stability analysis; Newmark-type approach; Factor of safety; Yield acceleration; Predictive models; Neural network

1. Introduction

Landslides are one of the most catastrophic consequences of earthquakes, as evidenced by many historical events in the past decades. Assessing the stability or performance of slopes under earthquake shaking is thus an important topic for both geotechnical practitioners and researchers. Among the current assessment approaches, the pseudo-static analysis and Newmark-type permanent-displacement analysis are most commonly used in the engineering practice (Bray and Travasarou 2009; Jibson 2011; Duncan et al. 2014; Kan et al. 2017; Ji et al. 2021, 2023). As shown in Fig. 1, the pseudo-static approach typically uses a seismic coefficient (k_h) to represent seismic loading in the calculation of factor of safety (FS) for the slope, whereas the Newmark-type approach estimates the permanent downslope-displacement of potential sliding mass during earthquake shaking.

While the pseudo-static approach can be implemented using numerical or analytical procedures such as finite element method (FEM) and limit equilibrium method (LEM) (e.g., Karray et al. 2018; Wang et al. 2023), these procedures usually require non-trivial slope modeling and the aid of commercial software. In contrast, a quick non-modeling estimation of FS is often preferred, especially in the preliminary slope design stages (e.g., Li et al. 2009; Sahoo and Shukla 2019). This can be achieved by using semi-empirical pseudo-static analysis tools such as the stability chart method as pioneered by Taylor (1937) and refined by many subsequent works (e.g., Majumdar 1971; Michalowski 2002; Qin and Chian 2018; Sahoo and Shukla 2019; Cui et al. 2022). As summarized in Table 1, the existing pseudo-static tools have specific forms and ranges of applicability, and several issues and/or shortcomings need to be addressed. First, the combined effects of seismic shaking and pore water conditions are not

56 considered, although rainfall before an earthquake can change the pore water pressure within
57 slopes and affect its stability. Second, the depth ratio (D) demonstrated in Fig. 1a has not been
58 included as input, but the depth of slip surface can be restricted by an underlying hard stratum
59 (Loukidis et al. 2003; Burgess et al. 2019). Third, the graphical formats of stability charts can
60 be inefficient when considering a large number of slope scenarios, such as multiple cases in
61 probabilistic stability analyses considering variability in soil properties (e.g., Javankhoshdel
62 and Bathurst 2014; Liu and Leung 2018), or in regional landslide screening analyses involving
63 thousands of geographic information system (GIS) grid cells (e.g., Saade et al. 2016; Qin et al.
64 2019). In this regard, semi-empirical slope stability tool with a mathematically explicit
65 equation is desirable.

66 The permanent-displacement analysis approach conceptualized by Newmark (1965) has
67 been extensively adopted to evaluate the seismic slope performance (e.g., Rathje and Bray 1999;
68 Rathje and Antonakos 2011; Bray and Macedo 2019; Macedo et al. 2020). The Newmark-type
69 approach requires the yield acceleration (k_y) and the thickness (h_{mass}) or fundamental period (T_s)
70 of failure mass (see Fig. 1b) as two key input parameters (Jibson 2011; Bray and Macedo 2023).
71 Although the infinite slope model can offer straightforward procedures to estimate k_y for a
72 quick regional landslide assessment (e.g., Wang and Rathje 2015), this approach predefines a
73 linear failure plane (i.e., predefines h_{mass}) and is not applicable to deep-seated landslides. It has
74 been documented that in addition to shallow landslides, seismically-induced deep landslides
75 exhibiting circular, spiral, or complex slip surfaces also occur across a large region (e.g., Jibson
76 and Michael 2009; Ma et al. 2019). Therefore, two-dimensional LEM and FEM are expected
77 to produce more reasonable results for slopes exhibiting various potential failure modes

78 (Duncan et al. 2014; Saade et al. 2016). Nonetheless, the formal implementation of LEM and
79 FEM in regional-scale analyses is usually hindered by the need for iterative processes with
80 high computational costs (Tsai et al. 2019). Alternatively, practical tools for k_y have been
81 developed as listed in Table 2, while most of them require a graphical inference and their
82 functionality needs improvement. Chien and Tsai (2017) suggested a predictive equation for
83 h_{mass} under the static conditions. However, failure surfaces could be considerably deeper in
84 seismic slope analyses (Leshchinsky and San 1994; Baker et al. 2006). It is therefore desirable
85 to develop more generalized predictive models of k_y and h_{mass} for both shallow and deep slope
86 failures under seismic conditions, which are also compatible with the recently developed,
87 flexible Newmark-type models (e.g., Rathje and Antonakos 2011; Bray and Macedo 2023).

88 The advancements in remote sensing, borehole databases, geostatistical models, and
89 landslide-inventory-based back-analysis methods have led to the increased availability of
90 geologic/geotechnical information at the regional scale (e.g., Rathje and Franke 2016; Liu et
91 al. 2017; Stewart et al. 2022; Gong et al. 2023). To take advantage of them, a key motivation
92 of this study is to refine the regional seismic landslide analysis approaches without
93 compromising computational efficiency. In addition, site-specific probabilistic slope stability
94 analyses usually require thousands of Monte Carlo simulation (MCS) samples (e.g., Li et al.
95 2016; Wang and Goh 2021). Therefore, another key motivation is to enable a practical tool for
96 probabilistic seismic slope stability assessment during the preliminary design phase. This is
97 helpful for practitioners to identify design parameters and reduce computational efforts in the
98 subsequent MCS-based formal LEM/FEM analyses. These motivations highlight the need to
99 develop powerful and generic surrogate models. Recently, machine learning (ML) techniques

100 have demonstrated promising ability in tackling geotechnical engineering problems (e.g., Lo
101 and Leung 2019; Wang et al. 2020; Ching et al. 2021, 2023). However, most existing ML
102 studies on slope stability predictions (e.g., Wang and Goh 2021; Lin et al. 2022;
103 Mahmoodzadeh et al. 2022; Pei et al. 2023) were conducted for static condition, and mainly
104 intended to demonstrate ML performance using relatively small datasets (i.e., with several
105 hundred or less data points). Instead, this study aims to develop generic predictive models of
106 seismic slope stability utilizing a comprehensive database, which can be directly applied to
107 efficiently identify high-risk zones at a regional scale and provide preliminary estimations of
108 slope failure probability within the MCS framework.

109 To achieve these goals, this paper proposes generic models for: (1) predicting seismic or
110 static *FS* and identifying the failure surface among shallow, toe, and deep modes; (2) predicting
111 k_y and the associated h_{mass} and h_{mass}/h_{tot}. Substantial efforts are conducted to establish a
112 comprehensive database based on 741,312 and 123,552 slope stability analyses for deriving *FS*
113 and k_y, respectively. The first two aforementioned issues of existing approaches are tackled in
114 this study by utilizing the comprehensive database and including both the pore pressure
115 coefficient (r_u) and depth ratio D as model inputs. The other inputs include k_h, slope angle (β),
116 slope height (H), and cohesion (c) and friction angle (ϕ) of soil. To represent the complex input-
117 output relationship without losing practicality, a neural network is introduced for establishing
118 an explicit predictive equation for each model. Both spreadsheet and MATLAB files are
119 provided to facilitate model applications. The performance of the proposed semi-empirical
120 models is systematically evaluated based on detailed comparisons with the exiting physics-
121 based models, as well as extensive blind tests involving thousands of slope configurations not

included in the training process. Finally, application of the developed models is illustrated by three examples.

2. Background and motivations

2.1. Quick estimations of *FS* and failure mode for pseudo-static analysis

Compared to formal FEM and LEM, a quick estimation of *FS* without numerical modeling (e.g., grid or slice division) can be preferable, especially in preliminary slope design stages. Based on circular slip surfaces, Taylor (1937) developed a set of slope stability charts for quick estimation of *FS*. Subsequent efforts have been made to largely eliminate the iterative process involved in the chart implementation, identify the type of failure mode, and account for external loadings (e.g., Michalowski 2002; Li et al. 2010; Qin and Chian 2018). Many of these previous endeavours focused on prediction of static slope stability only, and not the combined effects of earthquake shaking, pore water status, or the existence of underlying hard stratum (see Table 1). Moreover, the stability charts cannot be implemented as effectively as the programmable parametric predictive equations. This can become a significant hurdle in probabilistic stability analysis/design (involving a large number of geotechnical parameter randomizations and design scheme optimizations) and regional landslide screening (involving a large number of slope configurations).

One of the main purposes of this study is to develop mathematically explicit models for predicting *FS* and identifying slope failure mode. The failure mode identification will be equivalent to a classification problem with three target variables, which are the occurrence probabilities of shallow, toe, and deep modes (P_{shallow}, P_{toe}, and P_{deep}) as displayed in Fig. 1a.

2.2. Quick estimations of k_y and h_{mass} for Newmark-type displacement analysis

The Newmark-type approach can broadly be classified into the rigid-block analysis, decoupled analysis, and coupled analysis (Jibson 2011). These procedures require k_y and h_{mass} as input parameters (see Fig. 1b), where h_{mass} is used directly in analytical Newmark procedures (e.g., Rathje and Bray 1999; Kan et al. 2017), or indirectly to estimate T_s for semi-empirical Newmark procedures (e.g., Macedo et al. 2020; Bray and Macedo 2023). In addition, the distance between the top of failure mass and the hard stratum, i.e., the total thickness (h_{tot}) (see Fig. 1b), is also of importance in quantifying the dynamic response of slope below slip surface (e.g., Song et al. 2018).

These parameters are typically obtained from LEM or FEM through an iterative process, by searching for the critical k_h that results in FS=1 under the pseudo-static analysis framework (Jibson 2011). This process can be time-consuming, particularly for probabilistic slope displacement hazard analysis and regional seismic landslide hazard mapping (e.g., Tsai et al. 2019; Wang et al. 2021). Although the infinite slope model has been extensively used to estimate k_y in regional landslide assessments, this approach predefines a failure plane (i.e., a prior estimation of h_{mass}) and is not applicable to deep-seated landslides (Ducan et al. 2014). Following the same idea as the classical stability charts, a few efforts have been made to develop semi-empirical k_y predictive tools (as shown in Table 2). However, these tools suffer from similar limitations to those encountered by the pseudo-static analysis tools. Moreover, most of the tools cannot estimate h_{mass} (or h_{tot}), and improvements are needed on aspects such as accounting for pore-water pressure and the depth to hard stratum. This study will develop generalized predictive models for k_y, h_{mass}, and h_{tot}, respectively.

3. Comprehensive slope stability analyses and data preparation

This section presents extensive pseudo-static LEM analyses that are conducted to investigate the effects of external loading conditions (i.e., seismic shaking and pore-water pressure) and slope properties (i.e., slope angle and soil parameters) on the seismic slope stability indices, and to identify the key parameters in controlling the slope stability. The analysis results are then utilized to establish a comprehensive database for development of the semi-empirical predictive models.

3.1. Slope model configurations

Many existing stability charts and predictive models for FS and k_y were developed using a single combination of H and D (see Fig. 1), such as [H = 20 m, D = 1.5] (Loukidis et al. 2003), [H = 30 m, D = 3.3] (Saade et al. 2016), and [H = 5 m, D = 2] (Burgess et al. 2019). To achieve better generalization capability for the new predictive models, this study considers 12 generic slope geometry types by combining H = 5 m and 30 m with six D values (i.e., 1, 1.5, 2, 2.5, 3, and 3.5). The predictive models are normalized with respect to $c/(\gamma H)$ to further enhance their applicability (Michalowski 2002; Baker et al. 2006), such that various values of γ and H can be considered in future applications. The slope angle β is specified to range from 10° to 70° with increments of 5°. The shear strength of soils is modeled with the Mohr-Coulomb criterion using the cohesion (c) and friction angle (ϕ). The selected c and ϕ values are between 1 and 100 kPa with general increments of 10 kPa (i.e., 1, 10, 20, …, 100 kPa), and are between 5° and 60° with increments of 5°, respectively. These ranges have been chosen to be comparable or broader than those employed in previous studies, ensuring reasonable applicability in various engineering scenarios.

187 The pore pressure coefficient (r_u) is incorporated to account for pore water effects. This is
188 defined as (Bishop and Morgenstern 1960):

189 $$r_u = \frac{u}{\gamma z} \quad (1)$$

190 where z is the depth of the point on the slip surface; u is the pore water pressure. Although this
191 is a simplified description of the complex pore water distribution, r_u is often useful for practical
192 purposes (Michalowski 2002). In this study, r_u is selected from 0 to 0.5 with increments of 0.1.
193 To cover the typical earthquake shaking intensities (Bray and Travasarou 2009), k_h is
194 considered to vary from 0 to 0.5 with increments of 0.1. Based on these parameter combinations,
195 a large amount of pseudo-static stability analyses are performed through Bishop's simplified
196 method, resulting in 741,312 FS values (2 slopes × 13 β × 11 c × 12 ϕ × 6 D × 6 r_u × 6 k_h) and
197 123,552 k_y values (2 slopes × 13 β × 11 c × 12 ϕ × 6 D × 6 r_u), respectively. The failure mode
198 and h_{mass} for the critical slip surface are extracted from each analysis, where h_{mass} specifically
199 denotes the maximum thickness of failure mass (Bray and Macedo 2023).

200 **3.2. Results and physical interpretation**

201 Fig. 2 investigates the effects of slope properties and external loadings on FS, k_y, and the
202 associated critical slip surfaces considering 9 combinations of slope properties and 2 external
203 loading conditions, where D=3.5 is used to represent a deep hard stratum. Note that k_y="0"
204 represents the statically unstable slope case with no slip surface shown. It is observed that: (1)
205 the toe failure mode is most likely to be triggered in different scenarios; (2) larger ratio of c to
206 ϕ and smaller β generally result in larger volumes of failure masses (i.e., deeper and wider slip
207 surfaces); (3) the sliding volumes generally become larger with the increase of k_h, especially

for a larger ratio of c to ϕ, yet are marginally smaller for lower values of r_u; (4) as expected, larger k_h or r_u values lead to less stable slope conditions (i.e., lower FS or k_y).

The FS versus $c/(\gamma H)$ trends for some representative conditions (in terms of ϕ, β, k_h, r_u, and D) are illustrated in Fig. 3. Several observations can be made. First, the influence of β on FS is generally larger for larger ϕ and smaller k_h, especially when $c/(\gamma H)$ is relatively small. In these cases, the critical slip surfaces are relatively shallow as discussed above, such that the slope stability is more closely related to β. The effect of β gradually becomes smaller with increasing $c/(\gamma H)$ and is sufficiently small when $c/(\gamma H)$ exceeds a critical value. This critical value or equivalently the β effect within the typical $c/(\gamma H)$ range appears to be larger for smaller k_h or D (i.e., shallower slip surface as demonstrated in Fig. 2). Second, the effect of ϕ is more pronounced for smaller β. This may be because the normal force on slip surface would be generally larger for smaller β, which consequently enlarges the resisting force associated with the friction shear resistance of soils. For relatively large β, cohesion is important in affecting the slope stability.

Third, the difference between Fig. 3b and d illustrates that FS decreases with increasing D (deeper hard stratum). As D becomes larger, the potential failure zone would be extended, yielding more critical slope failure (i.e., smaller FS). Such influence is generally larger for smaller β due to the increased occurrence possibility of deeper slip surfaces. Fourth, increasing r_u results in lower FS, but the effect of r_u on the general variation of FS trend is relatively small (see Fig. 3b and c). This is not unexpected since r_u has considerable influence on the effective stress status along slip surface yet only marginally affects the failure surface location.

The parameter k_y should be constrained to the theoretical limiting value ($k_{y,lim}$) (Loukidis

et al. 2003; Burgess et al. 2019), which represents the special case of sliding along the boundary between soil and its underlying hard stratum. In other words, $k_{y,lim}$ corresponds to the pseudo-static horizontal acceleration required to initiate the sliding of the entire soil profile (with a thickness of HD). Hence, the value of $k_{y,lim}$ remains constant regardless of the different positions of potential slip surfaces within the slope. Since this study considers non-zero r_u, a slight modification is made to calculate $k_{y,lim}$ as:

$$k_{y,lim} = \left[\frac{c}{\gamma HD} + (1 - r_u) \tan\phi \right] \mathrm{g} \tag{2}$$

Consequently, the computed k_y values corresponding to $k_y > k_{y,lim}$ are set to $k_{y,lim}$. In the implementation of a predictive model, this modification is needed to prevent the predicted k_y from exceeding $k_{y,lim}$.

Furthermore, Fig. 4 compares the k_y versus $c/(\gamma H)$ trends for different values of ϕ, β, r_u, and D. It is observed that the shape of the k_y trends is generally similar to that for FS. The k_y values produced by different β values differ more evidently for larger ϕ. The difference gradually diminishes with the increase of $c/(\gamma H)$, and eventually k_y is not dependent on β, when $c/(\gamma H)$ exceeds a certain value (e.g., 0.2 for D = 3.5 or 0.3 for D = 1). On the other hand, the influence of ϕ on k_y is generally smaller for larger r_u or smaller D.

Some previous studies suggested that k_y can be used to approximately estimate the pseudo-static FS under specific k_h using the following formula (Baker et al. 2006):

$$F_{ky} = \frac{k_y}{k_h \mathrm{g}} \tag{3}$$

Based on our dataset, this approximation method is re-evaluated by comparing F_{ky} transformed from k_y with the actual FS computed directly from stability analysis in Fig. 5. It is seen that the

F_{ky} approximation using Eq. (3) generally produces significant deviation especially for k_h=0.1. Therefore, this method could lead to biased results in these cases. In contrast, it is more appropriate to predict *FS* directly, as will be shown in later sections of this paper.

3.3. Data preparation

The aforementioned slope stability results will be taken as training data to develop predictive models for *FS*, [$P_{shallow}$, P_{toe}, P_{deep}], k_y, and [h_{max}/H, h_{max}/h_{tot}], which are hereafter referred to as M-FS, M-P, M-KY, and M-H, respectively. For static *FS* less than 1 or k_y less than 0.005 g, the slope is essentially unstable in static condition (Wang and Rathje 2015). Therefore, the data for such statically unstable slope scenarios will not be used in the subsequent model development. Based on the investigations on influencing factors in Figs. 2-4, [$c/(\gamma H)$, tanϕ, tanβ, D, r_u, k_h] are selected as the predictors in the M-FS and M-P models, and [$c/(\gamma H)$, tanϕ, tanβ, D, r_u] are used for the M-KY and M-H models. Regarding the M-P model, one-hot encoding is used to prepare the categorical target data. For example, the targets are written as [1, 0, 0] and [0, 0, 1] for shallow and deep critical slip surfaces, respectively (see Fig. 1a). In addition, the target h_{max}/H and h_{max}/h_{tot} for the M-H model are extracted from each k_y calculation (see Fig. 1b).

To conduct blind test of model performance, a testing dataset built on thousands of new slope configurations with H=15 m and γ=19 kN/m^3 is established. The parameters c, ϕ, β, r_u, k_h, and D are specified as [1, 5, 15, …, 95 kPa], [7, 12, …, 52°], [15, 30, …, 60°], [0, 0.05, 0.15, …, 0.45], [0, 0.05, 0.15, …, 0.45], and [1, 1.5, …, 3.5], respectively. These parameter values are purposely set to be different from those of the training data (e.g., c = [1, 10, 20, …, 100 kPa] and r_u = [0, 0.1, …, 0.5]) to test the generalization capability of the model. More than 100,000 and 12,000 sets of data are produced by the *FS* and k_y calculations, respectively.

4. Novel generic predictive models for seismic slope stability indices

4.1. Artificial neural network proposed for slope stability prediction

A machine-learning algorithm with higher degree of complexity (e.g., more parameters) generally yields better predictive performance, yet enlarges the risk of overfitting and the difficulty in practical implementation. As a tradeoff between model performance and practicality, a neural network (e.g., Hastie et al. 2009) is adopted herein to develop the M-FS, M-P, M-KY, and M-H models. The choice of the neural network approach is based on its superior performance over the traditional polynomial regression approaches (e.g., Saade et al. 2016; Li et al. 2021) in our prior comparative study. Meanwhile, this work is not merely a "machine-learning fitting" exercise to demonstrate the performance of algorithms on specific geotechnical datasets. Instead, the target models and parameter ranges are designed for generic applications based on the established large database. Fig. 6a schematically illustrates a fully-connected network architecture consisting of an input layer, two hidden layers, and an output layer, where each hidden layer contains m neurons. According to preliminary sensitivity analyses, the double-hidden-layer architecture is specified for the M-FS and M-KY models, whereas a single hidden layer is used for the M-P and M-H models.

To reduce the numeric difference among different predictor variables, each parameter in $[x_1, x_2, \ldots, x_n] = [c/(\gamma H), \tan\phi, \tan\beta, D, r_u, k_h]$ (where $n = 6$) or $[c/(\gamma H), \tan\phi, \tan\beta, D, r_u]$ (where $n = 5$) is scaled into the $[L, U]$ range by the min-max normalization, expressed as:

$$\tilde{x}_i = (U - L)\frac{x_i - x_{i,\min}}{x_{i,\max} - x_{i,\min}} + L, \quad i = 1, 2, ..., n \tag{4}$$

where $\tilde{x}_i$ denotes the normalized predictor; L and U are set to -1 and 1, respectively; $x_{i,\min}$ and

$x_{i,\max}$ denote the minimum and maximum sample values of x_i, respectively, which are listed in Table 3.

As a result, the prediction can be explicitly expressed by simple matrix operations. For the M-FS or M-KY model, the target variable $y = \ln(FS)$ or $\ln(k_y)$ is predicted as:

$$\ln(FS) \text{ or } \ln(k_y) = y = f_1\left(f_1\left(\left[\tilde{x}_1, \tilde{x}_2, ..., \tilde{x}_n\right]\mathbf{w}_1 + \mathbf{b}_1\right)\mathbf{w}_2 + \mathbf{b}_2\right)\mathbf{w}_3 + b_3 \quad (5)$$

where $\mathbf{w}_1$, $\mathbf{w}_2$, and $\mathbf{w}_3$ are weight matrices with dimensions of n-by-m, m-by-m, and m-by-1, respectively; $\mathbf{b}_1$ and $\mathbf{b}_2$ denote 1-by-m bias vectors; b_3 is the output bias value; $f_1(\cdot)$ represents a tangent-sigmoid activation function applying operation to each element of a vector $\left[e_1, e_2, ..., e_m\right]$, which can be expressed as:

$$f_1\left(\left[e_1, e_2, ..., e_m\right]\right) = \left[\frac{2}{1+\exp(-2e_1)} - 1, \frac{2}{1+\exp(-2e_2)} - 1, ..., \frac{2}{1+\exp(-2e_m)} - 1\right] \quad (6)$$

The M-H model predicts two target variables $[y_1, y_2] = [\ln(h_{\text{mass}}/H), \ln(h_{\text{mass}}/h_{\text{tot}})]$ using only one hidden layer, and the prediction is written as:

$$\left[\ln\left(h_{\text{mass}}/H\right), \ln\left(h_{\text{mass}}/h_{\text{tot}}\right)\right] = f_1\left(\left[\tilde{x}_1, \tilde{x}_2, ..., \tilde{x}_n\right]\mathbf{w}_1 + \mathbf{b}_1\right)\mathbf{w}_2 + \mathbf{b}_2 \quad (7)$$

where the dimensions of $\mathbf{w}_2$ and $\mathbf{b}_2$ are changed into m-by-2 and 1-by-2, respectively.

In addition, the M-P model predicts $[y_1, y_2, y_3] = [P_{\text{shallow}}, P_{\text{toe}}, P_{\text{deep}}]$ as a function of:

$$\left[P_{\text{shallow}}, P_{\text{toe}}, P_{\text{deep}}\right] = f_2\left(f_1\left(\left[\tilde{x}_1, \tilde{x}_2, ..., \tilde{x}_n\right]\mathbf{w}_1 + \mathbf{b}_1\right)\mathbf{w}_2 + \mathbf{b}_2\right) \quad (8)$$

where $f_2(\cdot)$ is the softmax function that can be written as:

$$f_2\left(\left[e_1, e_2, e_3\right]\right) = \left[\frac{\exp(e_1)}{\sum_{k=1}^{3}\exp(e_k)}, \frac{\exp(e_2)}{\sum_{k=1}^{3}\exp(e_k)}, \frac{\exp(e_3)}{\sum_{k=1}^{3}\exp(e_k)}\right] \quad (9)$$

During the training process, the mean squared error is used as the performance metric (PM) for the M-FS, M-KY, and M-H models, whereas the cross entropy is taken as PM for the M-P model. The goal is to minimize PM as much as possible without causing undesirable overfitting.

315 **4.2. Model development**

316 For the proposed neural network architecture, *m* is taken as the hyperparameter. In this
317 subsection, a grid search method that integrates the *K*-fold cross validation with the early
318 stopping strategy is used to determine *m*, and the basic steps are summarized as follows:

319 (1) Split the training dataset (established in Section 3.3) into *K* subsets equally, and predefine
320 the candidate values of *m* (i.e., [2, 4, …, 50] in this study).

321 (2) For each candidate value of *m*, perform training of the neural network on all data in *K*-1
322 subsets with a large number of (e.g., 1000) epochs, and record PM evaluated on the
323 remaining one data subset.

324 (3) Repeat the previous step *K*-1 times to conduct *K* independent validation rounds (on *K* data
325 subsets), and then compute the average PM_{ave} of the resulting *K* values of PM for each
326 training epoch. Subsequently, the final number of training epochs and its associated PM_{ave}
327 are determined when there is an increase or no significant decrease (with a rate of change
328 less than 0.5%) in PM_{ave}, after increasing the epochs by 20.

329 (4) Repeat Steps (2)-(3) until all the candidate *m* values have been considered.

330 (5) Identify the optimal *m* value, which corresponds to the lowest PM_{ave} or when minor
331 variation of PM_{ave} results from further increasing *m*.

332 The identified optimal *m* values for the M-FS, M-KY, M-P, and M-H models are 46, 32,
333 26, and 18, respectively. These are subsequently used for the final model development, as
334 demonstrated in Fig. 6b. The resulting weight and bias values for Eq. (5), (7), and (8) are
335 presented in a spreadsheet file in Supplementary material. This spreadsheet file also allows for
336 direct implementation of the models as shown in Fig. 6c. Besides, the MATLAB scripts for

batch implementation are provided at https://github.com/MaoxinWang/predKyFS.

5. Evaluation of model performance

5.1. Residual analyses

The residuals of FS, k_y, $\ln(h_{mass}/H)$, and $\ln(h_{mass}/h_{tot})$ versus $c/(\gamma H)$ are displayed in Fig. 7. The means of residuals for individual $c/(\gamma H)$ values are shown in each plot. It is observed that the residual distributions of $\ln(h_{mass}/H)$ and $\ln(h_{mass}/h_{tot})$, which are both outputs from the M-H model, are quite similar. For the three models, the lack of evident biases in the mean trends indicates the favorable performance of the models, with generally unbiased predictions. Compared to h_{mass}/H and h_{mass}/h_{tot}, better predictability is observed for FS and k_y.

Based on the residual data, Fig. 8a presents the standard deviations of FS and k_y residuals with varying $c/(\gamma H)$. Meanwhile, the standard deviations of the $\ln(h_{mass}/H)$ and $\ln(h_{mass}/h_{tot})$ residuals are displayed in Fig. 8b. It is seen that the standard deviations vary notably with $c/(\gamma H)$. Specifically, the standard deviation of residuals for FS increases notably as $c/(\gamma H)$ approaches 0.2, and remains relatively constant for $c/(\gamma H) > 0.2$. In the other cases, the standard deviations of residuals generally increase at first, and decrease subsequently with increasing $c/(\gamma H)$.

To measure the uncertainty associated with slope stability prediction by the proposed models, the standard deviation of residuals is parametrized as a function of $c/(\gamma H)$ for potential applications. Because of their similarity, the standard deviations for $\ln(h_{mass}/H)$ and $\ln(h_{mass}/h_{tot})$ are averaged to yield a single equation. The results showed that the residuals of FS, k_y, and $\ln(h_{mass}/H)$ or $\ln(h_{mass}/h_{tot})$ can be approximately described by zero-mean normal distributions, where the standard deviations are respectively parametrized as:

$$\sigma_{FS} = \frac{-0.0061}{1+\exp\left[62.659\left(c/(\gamma H)-0.185\right)\right]} + 0.0088 \tag{10}$$

$$\sigma_{ky} = \frac{0.00154 - 0.0146\,c/(\gamma H) + 0.0579\,c^2/(\gamma H)^2}{1 - 6.352\,c/(\gamma H) + 6.716\,c^2/(\gamma H)^2 + 26.756\,c^3/(\gamma H)^3} \tag{11}$$

$$\sigma_{\ln h} = \frac{0.102 - 0.622\left(c/(\gamma H)\right)^{0.5} + 1.26\,c/(\gamma H) - 0.723\left(c/(\gamma H)\right)^{1.5}}{1 - 4.354\left(c/(\gamma H)\right)^{0.5} + 5.111\,c/(\gamma H) - 0.26\left(c/(\gamma H)\right)^{1.5}} \tag{12}$$

The three equations are also plotted in Fig. 8. It is seen that the empirical data of standard deviations are reasonably matched by the equations.

5.2. Model trends and comparison with previously reported results

The general *FS* trends produced by the M-FS model for different values of $c/(\gamma H)$, ϕ (=10°, 25°, 40°), β (=15°, 30°, 45°, 60°), r_u (=0, 0.25), k_h (=0, 0.3), and D (=2, 3.5) are presented in Fig. 9. Also, the predictions from the stability chart presented by Michalowski (2002) are shown for comparison. It is observed that *FS* increases consistently with increasing $c/(\gamma H\tan\phi)$, and the increasing trend is more evident for larger ϕ, smaller r_u, and smaller k_h. Larger values of D result in smaller *FS*, while the effect of D is only notable for k_h>0 and relatively high $c/(\gamma H\tan\phi)$ (e.g., >0.4). This is physically reasonable since higher seismic shaking intensity as well as more cohesive and less frictional soils tend to yield deeper failure surfaces, such that D would have larger influence on the failure surface location and the associated *FS*. On the other hand, the M-FS model trends generally match the Michalowski's charts given identical conditions. Yet, the advantages of the proposed model lie in the explicit prediction with a parametric equation, the consideration of D as a predictor, and the capability of simultaneously incorporating non-zero r_u and k_h.

The performance of the proposed M-KY model is illustrated in Fig. 10 by plotting the k_y

trends for different values of $c/(\gamma H)$, ϕ (=10°, 25°, 40°), β (=15°, 30°, 45°, 60°), r_u (=0, 0.5), and D (=1.5, 3.5). The results for r_u=0 and D=1.5 derived by Loukidis et al. (2003) using formal slope stability analyses are also shown. It is observed that the predicted k_y increases with increasing $c/(\gamma H\tan\phi)$, while the increasing rate of k_y changes abruptly when both $c/(\gamma H\tan\phi)$ and k_y are relatively large (e.g., $c/(\gamma H\tan\phi)$>0.3 and k_y>0.3 g). In this case, the effect of β on k_y is minor and different β values produce almost identical k_y versus $c/(\gamma H\tan\phi)$ trends. This observation is consistent with the empirical data trends (see Fig. 4), illustrating the favorable fitting performance of the M-KY model. In general, the established M-KY model captures the physics-based k_y trends of Loukidis et al. (2003) reasonably well.

5.3. Blind test on new slope configurations

The generalization capability of the four developed models is assessed by the testing dataset (prepared in Section 3.3), which is fully independent of the training process. In particular, the M-FS model and M-KY model are compared with the *FS* model proposed by Li et al. (2021) and the k_y model proposed by Chien and Tsai (2017), respectively, although the two previous models are only applicable to r_u=0. Fig. 11a presents the distributions of predicted *FS* versus target *FS* for the M-FS model (r_u≥0) and the Li et al. (2021) model (r_u=0), in which the data points for $c/(\gamma H)$>0.2 and $c/(\gamma H)$≤0.2 are distinguished. It is seen that the predicted *FS* by the proposed model is almost perfectly correlated with the target *FS*, as quantitatively evidenced by the Pearson's correlation coefficient (R) of 1 and the low mean absolute error (MAE). In contrast, large scattering of data is observed for the Li et al. (2021) model, and the associated MAE is significantly larger than that for the M-FS model.

Fig. 11b evaluates the performance of the M-KY model including a comparison with the

Chien and Tsai (2017) model. It is found that the predicted k_y from the M-KY model is in good agreement with the target k_y in the full range of $c/(\gamma H)$, resulting in $R > 0.995$ and MAE < 0.01. Although the Chien and Tsai (2017) model is also found to predict k_y reasonably well at $c/(\gamma H) \leq 0.2$, the predictions are biased at $c/(\gamma H) > 0.2$. Therefore, the new models not only achieve enlarged applicable range (e.g., $r_u \geq 0$), but also provide more reliable predictions.

Fig. 11c compares the predicted h_{mass}/H with the target h_{mass}/H. It can be seen that h_{mass}/H is captured reasonably well by the M-H model, though its predictability is worse than that of k_y. There are some outliers for $h_{mass}/H \approx 0.75$ especially in the $c/(\gamma H) > 0.2$ and $D \geq 2.5$ cases, and the biases are mainly associated with the $k_y > k_{y,lim}$ cases and the moderate-to-deep slip surfaces. More efforts are needed for refined h_{mass} prediction. Furthermore, the performance of the M-P model is illustrated in Fig. 11d by the confusion matrix. The accuracy rates of prediction for all failure mode classes are observed to be higher than 80%, and the total accuracy rate is as high as 91%.

6. Application of the proposed models

Fig. 12 illustrates the potential applications of the proposed generic predictive models. The M-FS and M-P models are designed for regional/site-specific pseudo-static stability analyses, whereas the M-KY and M-H models are designed for regional/site-specific Newmark-type displacement analyses. This work should be useful for both practitioners and researchers, given that the pseudo-static analysis, Newmark-type analysis, and stress-deformation analysis are the three major seismic slope stability assessment approaches (Jibson 2011). It should be noted that this study does not intend to replace the infinite slope model, but provides a supplementary tool for cases where an explicit consideration of deep-seated landslides is required. The tool

422 can be employed in conjunction with the infinite slope model for regions involving both deep
423 and shallow landslides (e.g., Jibson and Michael 2009). The potential of the new tool is
424 expected to become larger with increasing availability of regional geologic/geotechnical
425 information as continuously promoted by various researchers in multiple fields.

426 Besides, the developed models can also be adopted to make a quick site-specific estimation
427 of FS, k_y, or slope failure probability in preliminary design/project stages. This is beneficial for
428 the subsequent, more computationally demanding, formal probabilistic/reliability assessments
429 of slope stability (e.g., Griffiths and Fenton 2004; Wang et al. 2021), in which thousands of
430 LEM or FEM runs via commercial software are often involved. Using our proposed tools for
431 probabilistic-based design, practitioners only need to change the inputted values of H, β, and
432 D for representing different design schemes (regarding slope geometry). The preliminary
433 results can be used to narrow down the ranges of these geometric parameters for the subsequent
434 detailed design phase, thereby reducing the efforts for repeated slope modeling (e.g., grid or
435 slice division) and stability analyses. It should also be noted that the predictive models are
436 conceptually compatible with the existing semi-empirical tools for pseudo-static coefficient
437 selection (e.g., Bray and Travasarou 2009; Macedo and Candia 2020) and slope displacement
438 prediction (e.g., Rathje and Antonakos 2011; Bray and Macedo 2019), as shown in Fig. 12.
439 Example applications of the proposed models are presented in the following subsections.

440 **6.1. Example I: Pseudo-static slope stability analysis**

441 The proposed M-FS and M-P models are applied to a slope example outlined in Baker et al.
442 (2006). As shown in Fig. 13a, the slope with geometry of H=7 m, β=40°, and D=1 is subjected
443 by the seismic loading of k_h=0.2 considering no pore water pressure (i.e., r_u=0). The soil

parameters are specified as c=10 kPa, ϕ=28°, and γ=18 kN/m^3. The detailed steps of estimating FS and [$P_{shallow}$, P_{toe}, P_{deep}] are as follows:

(1) Substitute $\boldsymbol{x} = \left[c/(\gamma H), \tan\phi, \tan\beta, D, r_u, k_h\right]$ into Eq. (4), resulting in $\tilde{\boldsymbol{x}}$ = [-0.860, -0.460, -0.485, -1, -1, -0.2].

(2) Substitute $\tilde{\boldsymbol{x}}$ into Eq. (5) with the weight and bias coefficients for the M-FS model, resulting in the output of FS = 1.11. Regarding the failure mode prediction, [$P_{shallow}$, P_{toe}, P_{deep}] = [0,0.997,0.003] can be obtained by substituting $\tilde{\boldsymbol{x}}$ into Eq. (8) with the weight and bias coefficients for the M-P model.

The predicted FS and failure mode agree with the reported FS = 1.11 and critical slip surface location in Baker et al. (2006), as displayed in Fig. 13a.

6.2. Example II: Seismic slope displacement analysis

A slope example from Loukidis et al. (2003) is used to illustrate the proposed M-KY and M-H models. As shown in Fig. 13b, the slope has H=25 m, β=18.43°, D=2, and r_u = 0.5. The soil parameters are specified as c=25 kPa, ϕ=30°, and γ=20 kN/m^3. The detailed steps of estimating k_y, h_{mass}, and h_{tot} are as follows:

(1) Substitute $\boldsymbol{x} = \left[c/(\gamma H), \tan\phi, \tan\beta, D, r_u\right]$ into Eq. (4), and $\tilde{\boldsymbol{x}}$ = [-0.913, -0.404, -0.878, -0.2, 1] is obtained.

(2) Substitute $\tilde{\boldsymbol{x}}$ into Eq. (5) with the weight and bias coefficients for M-KY, and the output is obtained as k_y = 0.128 g. In addition, [h_{mass}/H, h_{mass}/h_{tot}] = [0.62, 0.38] are obtained by substituting $\tilde{\boldsymbol{x}}$ into Eq. (7) with the weight and bias coefficients for M-H. Therefore, h_{mass} is estimated as 0.62H = 15.5 m, and h_{tot} is then obtained as h_{mass}/0.38 = 40.8 m.

The predicted results are similar to k_y = 0.127 g and [h_{mass}=15.5 m, h_{tot}=42 m] as reported

in Loukidis et al. (2003). To estimate the seismically-induced slope displacement (Jibson 2011), the soil shear wave velocity (V_s) is specified as 300 m/s, resulting in $T_s = 4h_{mass}/V_s = 0.21$ s. The slope is assumed to be located on a stiff soil site at a distance of 10 km from a strike-slip fault with moment magnitude (M_w) of 7.5. The [M_w, $SA(1.3T_s)$] model of Bray and Macedo (2018) and the [PGA, PGV, T_m] model of Song et al. (2018) are adopted for slope displacement prediction, where $SA(1.3T_s)$, PGA, PGV, and T_m represent spectral acceleration at the period of $1.3T_s$ (i.e., 0.21 s in this example), peak ground acceleration, peak ground velocity, and mean period, respectively. The ground-motion model developed by Rathje et al. (2004) is used to estimate T_m, whereas the other three ground-motion parameters are estimated by the Campbell and Bozorgnia (2014) model.

The median displacement is predicted as 13.4 cm from the [M_w, $SA(1.3T_s)$] model. On the other hand, the [PGA, PGV, T_m] model requires the site period (T_{site}) rather than T_s as an input, in which $T_{site} = 4h_{tot}/V_s$ is estimated as 0.54 s. Besides, h_{mass}/h_{tot} is needed as an additional parameter to account for the effect of site condition below slip surface. As a result, the median displacement is 13.9 cm from the [PGA, PGV, T_m] model. Although not demonstrated herein, the proposed M-KY and M-H models can also be incorporated into probabilistic seismic slope displacement hazard analyses accounting for multiple sources of uncertainty (Li et al. 2020; Macedo et al. 2020; Wang et al. 2021).

6.3. Example III: Probabilistic slope stability analysis

In addition to deterministic analysis, probabilistic slope stability analysis can be efficiently conducted by the proposed M-FS model with MCS. Since the model serves as a generic surrogate model, the MCS process will only take a matter of seconds regardless of the statistical

488 distributions of parameters (soil strength or external loading). In this subsection, the M-FS
489 model is used to reproduce the probabilistic static slope stability charts in Javankhoshdel and
490 Bathurst (2014) for $\beta = 45°$, $\mu_c/(\gamma H) = [0.05, 0.075, 0.1]$, $\mu_\phi = [20°, 25°, \ldots, 45°]$, $COV_c = 0.5$,
491 and $COV_\phi = 0.2$, where μ_c and COV_c (or μ_ϕ and COV_ϕ) represent the mean and coefficient of
492 variation of c (or ϕ), respectively. The failure probabilities versus μ_ϕ for the three $\mu_c/(\gamma H)$ cases
493 are presented in Fig. 14. The almost perfect agreement between the predicted results (k_h=r_u =0)
494 and the charts indicate the excellent performance of the M-FS model. Furthermore, the
495 proposed model can incorporate nonzero k_h and r_u, which are not considered in the
496 Javankhoshdel and Bathurst (2014) charts.

497 **7. Summary and conclusions**

498 The relationships between slope properties and seismic slope stability indices were investigated
499 through 741,312 and 123,552 pseudo-static limit equilibrium calculations of FS and k_y,
500 respectively. Based on the newly compiled datasets and artificial neural network, this paper
501 proposes generic predictive models for: (1) seismic or static FS (i.e., M-FS model) and the
502 category of associated slope failure mode (i.e., M-P model); and (2) k_y (i.e., M-KY model) and
503 the thickness of associated failure mass (i.e., M-H model). Compared with previous studies and
504 other existing methods, the proposed models incorporate the following new features: (i)
505 accounting for the effects of both seismic shaking and pore water pressure; (ii) allowing for
506 adjustable constraint on failure surface depth; (iii) extending the range of applicable slope
507 conditions; and (iv) providing explicit parametric equations for convenient automatic
508 implementation.

509 Comprehensive slope stability analysis results indicated that the slip surfaces generally

become deeper for larger $c/\tan(\phi)$, smaller β, and larger k_h, while increasing r_u slightly reduces the depth of slip surface. Meanwhile, the effect of β on FS or k_y is generally more pronounced for larger ϕ (and smaller k_h regarding k_y), especially when $c/(\gamma H)$ is relatively small, whereas the effect of ϕ is stronger for smaller β. Also, larger r_u and D generally result in lower FS or k_y, so conventional slope stability charts or models that neglect these two parameters could lead to unconservative estimates. The performance of the developed models is evaluated on both the training data and blind test data. The results illustrated that the proposed models not only produce physically reasonable trends, but also reduce the prediction bias and variance compared to the existing models.

The established models were applied to three examples for seismic slope stability and displacement assessments, where only a few seconds were needed even for the MCS-based probabilistic analyses. The M-FS and M-P models involve [$c/(\gamma H)$, $\tan\phi$, $\tan\beta$, D, r_u, k_h] as predictors, whereas [$c/(\gamma H)$, $\tan\phi$, $\tan\beta$, D, r_u] are used as predictors by the M-KY and M-H models. These parameters are all common in geotechnical practice. The proposed models can be implemented by: 1) simple matrix manipulation with the coefficients provided in Supplementary material, or 2) the supplementary spreadsheet file, or 3) the MATLAB scripts provided at https://github.com/MaoxinWang/predKyFS. These can serve as useful tools for engineers and researchers to perform quick assessments of seismic slope stability/performance on both site-specific and regional scales.

Data Availability Statement

Some or all data, models, or code that support the findings of this study are available from the corresponding author upon reasonable request.

Acknowledgments

The work presented in this paper is financially supported by the Research Grants Council of Hong Kong Special Administrative Region (Project No. 15222021).

Supplementary Materials

Supplementary spreadsheet file for implementing the proposed models is available with the article. Alternative MATLAB scripts for the batch implementation of models are available at https://github.com/MaoxinWang/predKyFS.

References

Baker, R., Shukha, R., Operstein, V., Frydman, S. (2006). Stability charts for pseudo-static slope stability analysis. Soil Dynamics and Earthquake Engineering, 26(9), 813-823.

Bishop, A. W., Morgenstern, N. (1960). Stability coefficients for earth slopes. Géotechnique, 10(4), 129-153.

Bray, J. D., Macedo, J. (2019). Procedure for estimating shear-induced seismic slope displacement for shallow crustal earthquakes. Journal of Geotechnical and Geoenvironmental engineering, 145(12), 04019106.

Bray, J. D., Macedo, J. (2023). Performance-based seismic assessment of slope systems. Soil Dynamics and Earthquake Engineering, 168, 107835.

Bray, J. D., Travasarou, T. (2009). Pseudostatic coefficient for use in simplified seismic slope stability evaluation. Journal of Geotechnical and Geoenvironmental Engineering, 135(9), 1336-1340.

Burgess, J., Fenton, G. A., Griffiths, D. V. (2019). Probabilistic seismic slope stability analysis and design. Canadian Geotechnical Journal, 56(12), 1979-1998.

554 Campbell, K. W., Bozorgnia, Y. (2014). NGA-West2 ground motion model for the average
555 horizontal components of PGA, PGV, and 5% damped linear acceleration response spectra.
556 Earthquake Spectra, 30(3), 1087-1115.
557 Chien, Y. C., Tsai, C. C. (2017). Immediate estimation of yield acceleration for shallow and
558 deep failures in slope-stability analyses. International Journal of Geomechanics, 17(7),
559 04017009.
560 Ching, J., Phoon, K. K., Ho, Y. H., Weng, M. C. (2021). Quasi-site-specific prediction for
561 deformation modulus of rock mass. Canadian Geotechnical Journal, 58(7), 936-951.
562 Ching, J., Phoon, K. K., Huang, P. (2023). Detection of outliers with respect to a MUSIC
563 geotechnical database. Canadian Geotechnical Journal, https://doi.org/10.1139/cgj-2023-
564 0188.
565 Cui, H., Ji, J., Song, J., Huang, W. (2022). Limit state line-based seismic stability charts for
566 homogeneous earth slopes. Computers and Geotechnics, 146, 104749.
567 Duncan, J. M., Wright, S. G. Brandon, L. T. (2014). Soil strength and slope stability. New York,
568 NY, USA: Wiley.
569 Gong, W., Zekkos, D., Clark, M. (2023). A pseudo-3D methodology for regional-scale back-
570 analysis of earthquake-induced landslides. Engineering Geology, 325, 107277.
571 Griffiths, D. V., Fenton, G. A. (2004). Probabilistic slope stability analysis by finite elements.
572 Journal of Geotechnical and Geoenvironmental Engineering, 130(5), 507-518.
573 Hastie, T., R. Tibshirani, J. Friedman. (2009). The elements of statistical learning. 2nd ed. New
574 York: Springer.
575 Javankhoshdel, S., Bathurst, R. J. (2014). Simplified probabilistic slope stability design charts

for cohesive and cohesive-frictional (c-ϕ) soils. Canadian Geotechnical Journal, 51(9), 1033-1045.

Ji, J., Wang, C. W., Gao, Y., Zhang, L. (2021). Probabilistic investigation of the seismic displacement of earth slopes under stochastic ground motion: a rotational sliding block analysis. Canadian Geotechnical Journal, 58(7), 952-968.

Ji, J., Zhang, W., Zhang, T., Song, J. (2023). Seismic displacement of earth slopes incorporating co-seismic accumulation of dynamic pore water pressure. Earthquake Engineering and Structural Dynamics, 52(6), 1884-1907.

Jibson, R. W. (2011). Methods for assessing the stability of slopes during earthquakes—A retrospective. Engineering Geology, 122(1-2), 43-50.

Jibson, R. W., Michael, J. A. (2009). Maps showing seismic landslide hazards in Anchorage, Alaska (p. 3077). Reston, VA, USA: US Geological Survey.

Kan, M. E., Taiebat, H. A., Taiebat, M. (2017). Framework to assess Newmark-type simplified methods for evaluation of earthquake-induced deformation of embankments. Canadian Geotechnical Journal, 54(3), 392-404.

Karray, M., Hussien, M. N., Delisle, M. C., Ledoux, C. (2018). Framework to assess pseudo-static approach for seismic stability of clayey slopes. Canadian Geotechnical Journal, 55(12), 1860-1876.

Leshchinsky, D., San, K. C. (1994). Pseudostatic seismic stability of slopes: Design charts. Journal of Geotechnical Engineering, 120(9), 1514-1532.

Li, A. J., Lyamin, A. V., Merifield, R. S. (2009). Seismic rock slope stability charts based on limit analysis methods. Computers and Geotechnics, 36(1-2), 135-148.

598 Li, A. J., Merifield, R. S., Lyamin, A. V. (2010). Three-dimensional stability charts for slopes
599 based on limit analysis methods. Canadian Geotechnical Journal, 47(12), 1316-1334.
600 Li, C., Su, L., Liao, H., Zhang, C., Xiao, S. (2021). Modeling of rapid evaluation for seismic
601 stability of soil slope by finite element limit analysis. Computers and Geotechnics, 133,
602 104074.
603 Li, D. Q., Wang, M. X., Du, W. (2020). Influence of spatial variability of soil strength
604 parameters on probabilistic seismic slope displacement hazard analysis. Engineering
605 Geology, 276, 105744.
606 Li, D. Q., Zheng, D., Cao, Z. J., Tang, X. S., Phoon, K. K. (2016). Response surface methods
607 for slope reliability analysis: review and comparison. Engineering Geology, 203, 3-14.
608 Lin, S., Zheng, H., Han, B., Li, Y., Han, C., Li, W. (2022). Comparative performance of eight
609 ensemble learning approaches for the development of models of slope stability prediction.
610 Acta Geotechnica, 17(4), 1477-1502.
611 Liu, W. F., Leung, Y. F. (2018). Characterising three-dimensional anisotropic spatial correlation
612 of soil properties through in situ test results. Géotechnique, 68(9), 805-819.
613 Liu, W. F., Leung, Y. F., Lo, M. K. (2017). Integrated framework for characterization of spatial
614 variability of geological profiles. Canadian Geotechnical Journal, 54(1), 47-58.
615 Lo, M. K., Leung, Y. F. (2019). Bayesian updating of subsurface spatial variability for improved
616 prediction of braced excavation response. Canadian Geotechnical Journal, 56(8), 1169-
617 1183.
618 Loukidis, D., Bandini, P., Salgado, R. (2003). Stability of seismically loaded slopes using limit
619 analysis. Géotechnique, 53(5), 463-479.

620 Ma, N., Wang, G., Kamai, T., Doi, I., Chigira, M. (2019). Amplification of seismic response of
621 a large deep-seated landslide in Tokushima, Japan. Engineering Geology, 249, 218-234
622 Macedo, J., Candia, G. (2020). Performance-based assessment of the seismic pseudo-static
623 coefficient used in slope stability analysis. Soil Dynamics and Earthquake Engineering,
624 133, 106109.
625 Macedo, J., Candia, G., Lacour, M., Liu, C. (2020). New developments for the performance-
626 based assessment of seismically-induced slope displacements. Engineering Geology, 277,
627 105786.
628 Majumdar, D. K. (1971). Stability of soil slopes under horizontal earthquake force.
629 Géotechnique, 21(1), 84-88.
630 Mahmoodzadeh, A., Mohammadi, M., Farid Hama Ali, H., Hashim Ibrahim, H., Nariman
631 Abdulhamid, S., Nejati, H. R. (2022). Prediction of safety factors for slope stability:
632 comparison of machine learning techniques. Natural Hazards, 1-29.
633 Michalowski, R. L. (2002). Stability charts for uniform slopes. Journal of Geotechnical and
634 Geoenvironmental Engineering, 128(4), 351-355.
635 Newmark, N. M. (1965). Effects of earthquakes on dams and
636 embankments. Géotechnique, 15(2), 139-160.
637 Pei, T., Qiu, T., Shen, C. (2023). Applying knowledge-guided machine learning to slope
638 stability prediction. Journal of Geotechnical and Geoenvironmental Engineering, 149(10),
639 04023089.
640 Qin, C., Chian, S. C. (2018). New perspective on seismic slope stability analysis. International
641 Journal of Geomechanics, 18(7), 06018013.

642 Qin, Y., Tang, H., Deng, Q., Yin, X., Wang., D. (2019). Regional seismic slope assessment
643 improvements considering slope aspect and vertical ground motion. Engineering Geology,
644 259, 105148.
645 Rathje, E. M., Antonakos, G. (2011). A unified model for predicting earthquake-induced sliding
646 displacements of rigid and flexible slopes. Engineering Geology, 122(1-2), 51-60.
647 Rathje, E. M., Bray, J. D. (1999). An examination of simplified earthquake-induced
648 displacement procedures for earth structures. Canadian Geotechnical Journal, 36(1), 72-
649 87.
650 Rathje, E. M., Faraj, F., Russell, S., Bray, J. D. (2004). Empirical relationships for frequency
651 content parameters of earthquake ground motions. Earthquake Spectra, 20(1), 119-144.
652 Rathje, E. M., Franke, K. (2016). Remote sensing for geotechnical earthquake reconnaissance.
653 Soil Dynamics and Earthquake Engineering, 91, 304-316.
654 Saade, A., Abou-Jaoude, G., Wartman, J. (2016). Regional-scale co-seismic landslide
655 assessment using limit equilibrium analysis. Engineering Geology, 204, 53-64.
656 Sahoo, P. P., Shukla, S. K. (2019). Taylor's slope stability chart for combined effects of
657 horizontal and vertical seismic coefficients. Géotechnique, 69(4), 344-354.
658 Song, J., Gao, Y., Feng, T., Xu, G. (2018). Effect of site condition below slip surface on
659 prediction of equivalent seismic loading parameters and sliding displacement.
660 Engineering Geology, 242, 169-183.
661 Stewart, J., Asimaki, D., Rathje, E. M., Bullock, Z., Ojomo, O., Wang, P., Zimmaro, P. (2022).
662 Framework for regional analysis of spatially distributed ground failure displacement
663 hazards.

Tang, G. P., Zhao, L. H., Li, L., Yang, F. (2015). Stability charts of slopes under typical conditions developed by upper bound limit analysis. Computers and Geotechnics, 65, 233-240.

Taylor, D.W. (1937). Stability of earth slopes. Journal of the Boston Society of Civil Engineers, 24, 197-247.

Tsai, H. Y., Tsai, C. C., Chang, W. C. (2019). Slope unit-based approach for assessing regional seismic landslide displacement for deep and shallow failure. Engineering Geology, 248, 124-139.

Wang, M. X., Huang, D., Wang, G., Li, D. Q. (2020). SS-XGBoost: A machine learning framework for predicting Newmark sliding displacements of slopes. Journal of Geotechnical and Geoenvironmental Engineering, 146(9), 04020074.

Wang, M. X., Li, D. Q., Du, W. (2021). Probabilistic seismic displacement hazard assessment of earth slopes incorporating spatially random soil parameters. Journal of Geotechnical and Geoenvironmental Engineering, 147(11), 04021119.

Wang, M. X., Wu, Q., Li, D. Q., Du, W. (2023). Numerical-based seismic displacement hazard analysis for earth slopes considering spatially variable soils. Soil Dynamics and Earthquake Engineering, 171, 107967.

Wang, Y., Rathje, E. M. (2015). Probabilistic seismic landslide hazard maps including epistemic uncertainty. Engineering Geology, 196, 313-324.

Wang, Z. Z., Goh, S. H. (2021). Novel approach to efficient slope reliability analysis in spatially variable soils. Engineering Geology, 281, 105989.

List of Figures

(a)

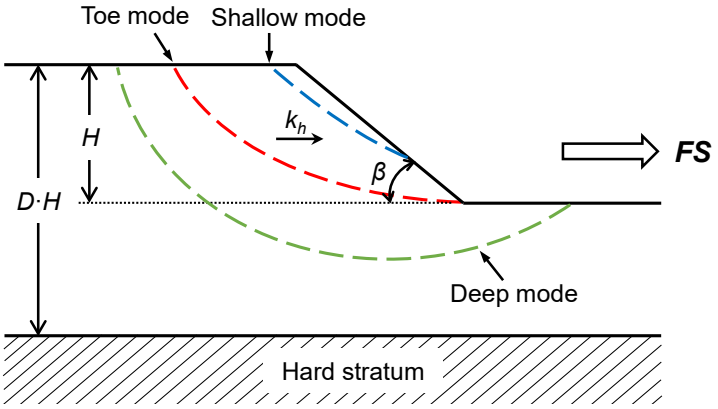

(b)

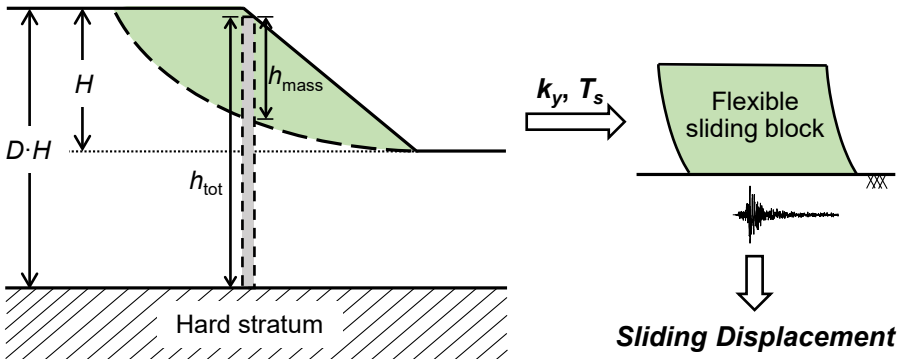

Fig. 1. Schematic illustrations of (a) pseudo-static slope stability analysis and (b) Newmark-type permanent-displacement analysis.

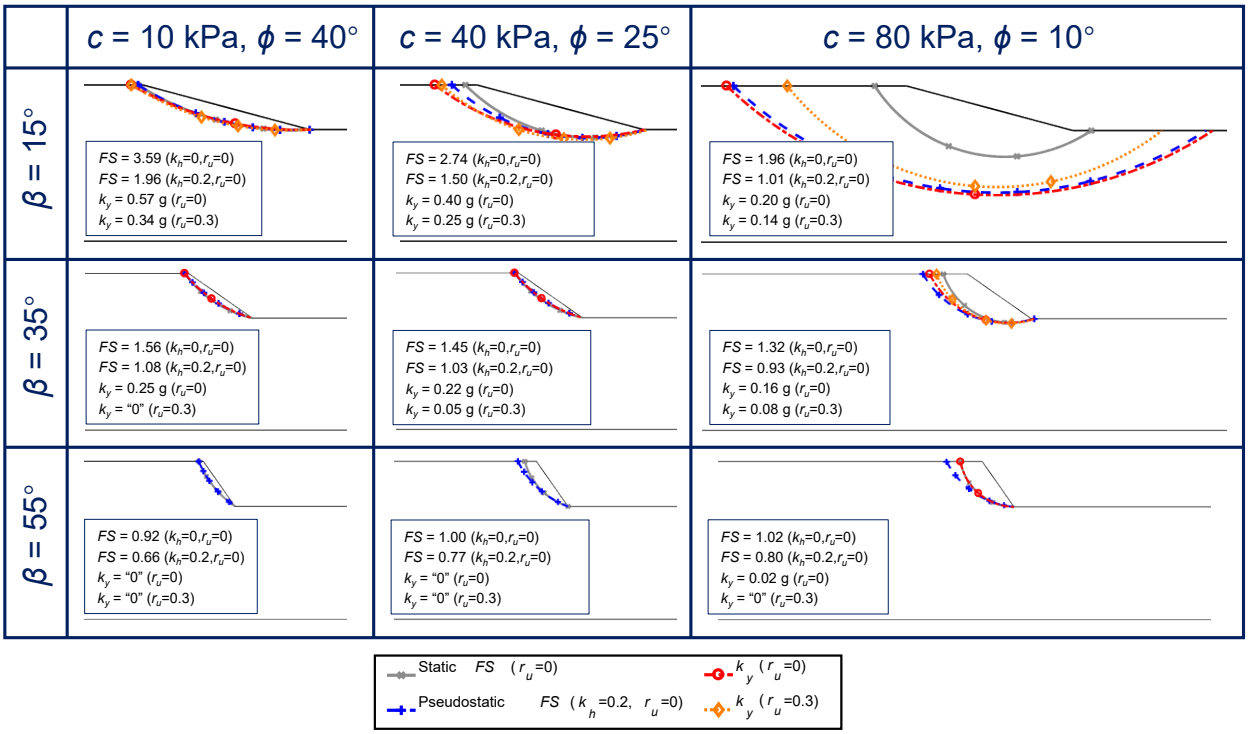

694

695 **Fig. 2.** Critical slip surfaces and associated stability analysis results under different slope property and

696 external loading conditions. The parameter *D* is specified as 3.5.

697

698 (a) (b)

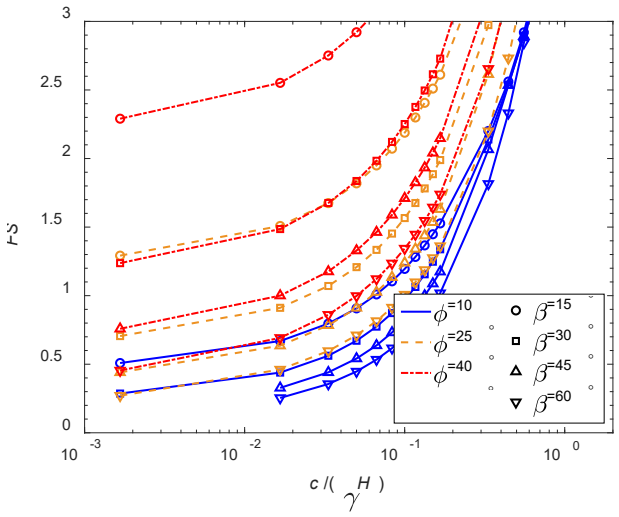

699

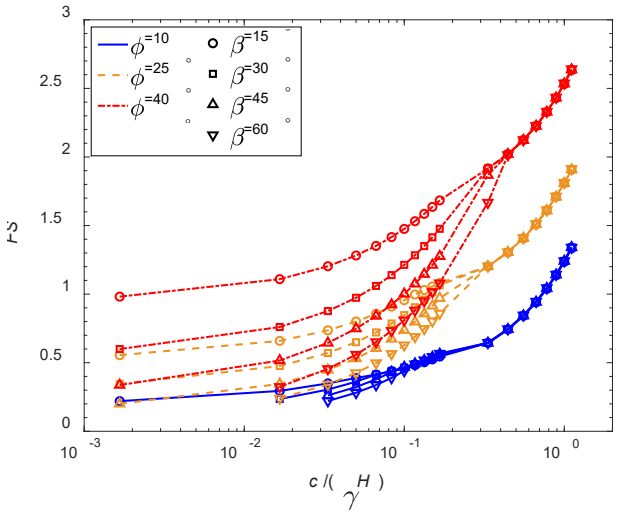

700

701 (c) (d)

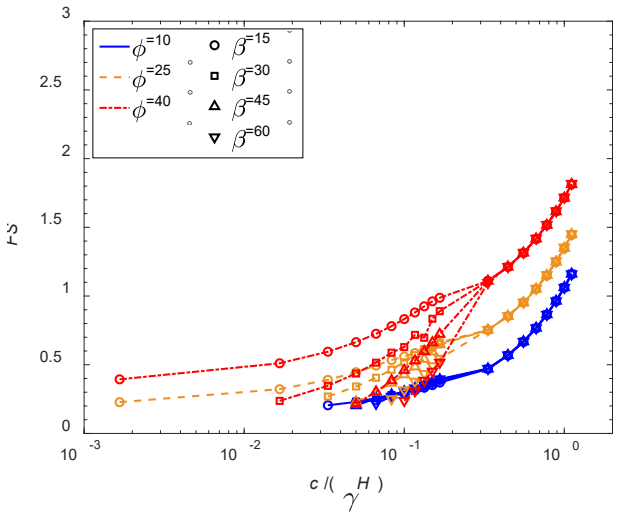

702

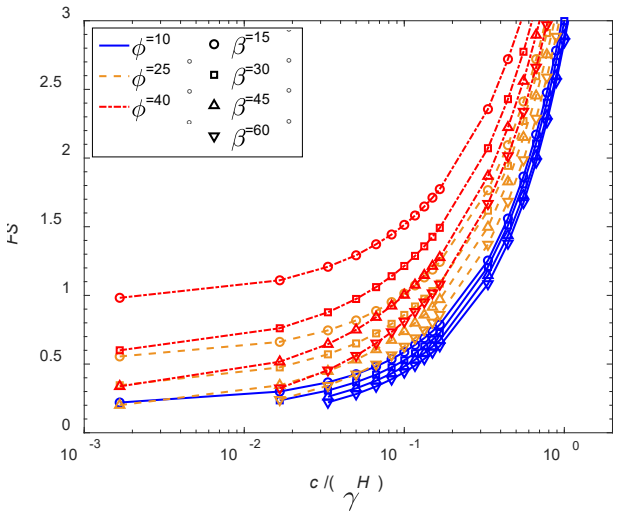

703

704 **Fig. 3.** Computed *FS* versus $c/(\gamma H)$ trends for different ϕ and β values in four scenarios: (a) [$k_h = 0.1$, $r_u = 0$,

705 $D = 3.5$]; (b) [$k_h = 0.5$, $r_u = 0$, $D = 3.5$]; (c) [$k_h = 0.5$, $r_u = 0.5$, $D = 3.5$]; and (d) [$k_h = 0.5$, $r_u = 0$, $D = 1$].

706 (a) (b)

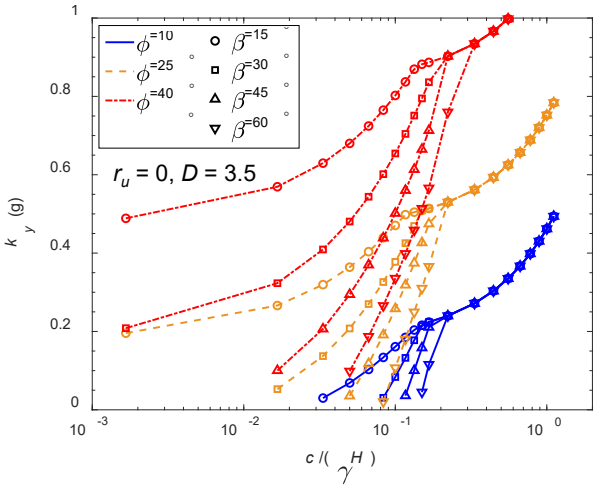

707

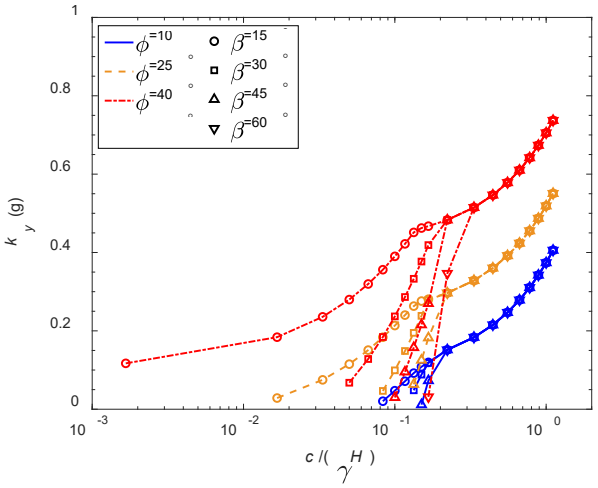

708

709 (c) (d)

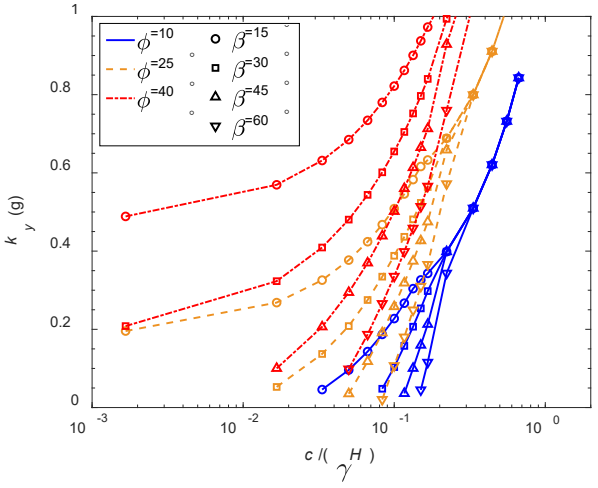

710

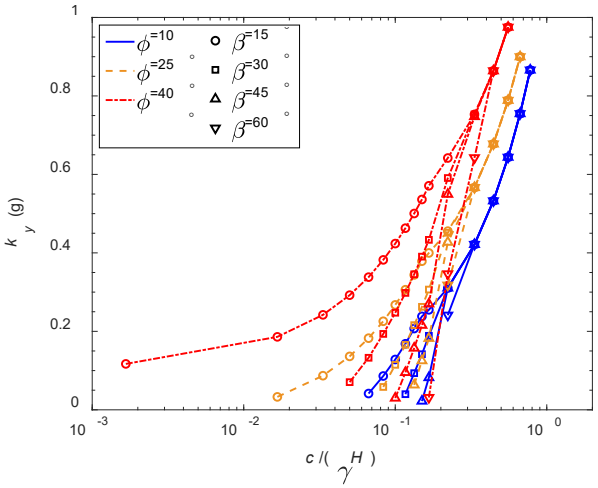

711

712 **Fig. 4.** Computed k_y versus $c/(\gamma H)$ trends for different ϕ and β values in four scenarios: (a) [$r_u = 0$, $D = 3.5$];

713 (b) [$r_u = 0.5$, $D = 3.5$]; (c) [$r_u = 0$, $D = 1$]; and (d) [$r_u = 0.5$, $D = 1$].

714

715 (a) (b)

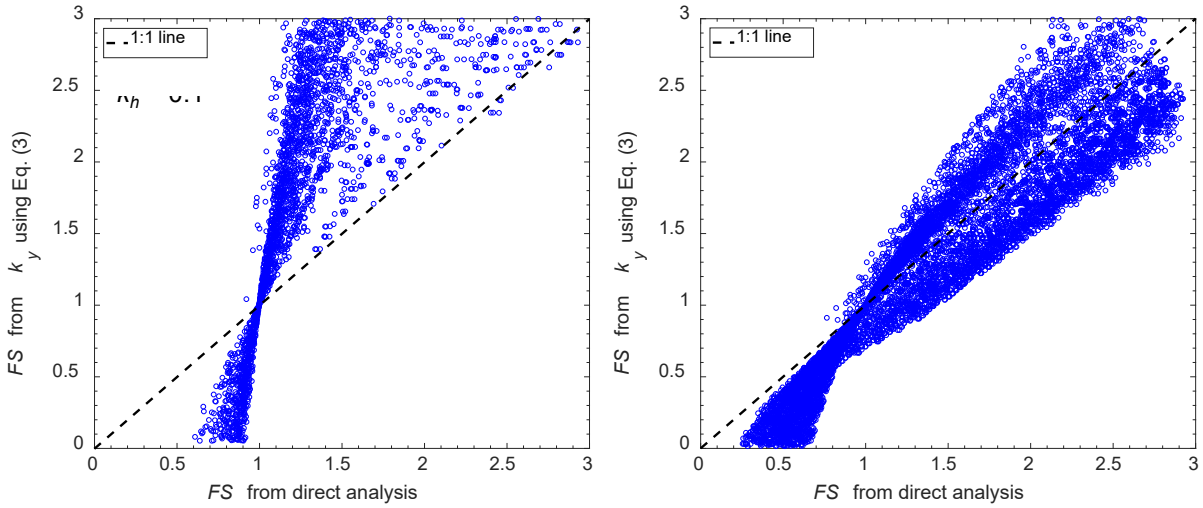

716

717 **Fig. 5.** Comparison of *FS* obtained from k_y transformation and direct PSLE analysis for (a) $k_h = 0.1$ and (b)

718 $k_h = 0.4$.

719 (a)

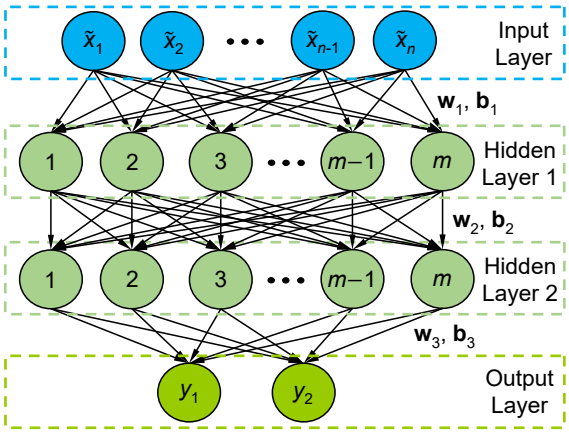

(b)

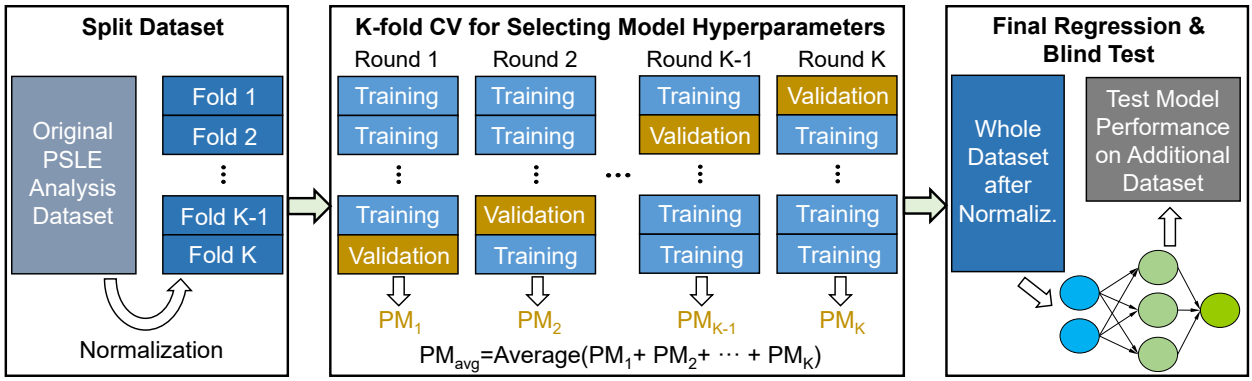

(c)

Predict factor of safety (FS) for static or pseudo-static slope stability analysis

INPUT (User-defined)							
c, cohesi	Gamma,	H, slope	Phi, friction	Beta, slo	D, depth	ru (pore	kh (seism
10	18	7	28	40	1	0	0.2

ANN Input (Automatic)					
x1=c/(γH	x2=tan(ph	x3=tan(B	x4=D	x5=ru	x6=kh
0.07937	0.53171	0.8391	1	0	0.2

OUTPUT (Automatic)	
FS	Std. Dev.
1.1109	0.0027

x1_min	x2_min	x3_min	x4_min	x5_min	x6_min
0.0017	0.0875	0.1763	1.0000	0.0000	0.0000

x1_max	x2_max	x3_max	x4_max	x5_max	x6_max
1.1111	1.7321	2.7475	3.5000	0.5000	0.5000

FS_min	FS_max
0.0000	5.0000

Normalized Input (Automatic)						
x1^tilde	x2^tilde	x3^tilde	x4^tilde	x5^tilde	x6^tilde	Raw FS
-0.8599	-0.4598	-0.4845	-1	-1	-0.2	1.1109

w1	Col 1	Col 2	Col 46
Row 1	-0.1477	-0.0290	-0.2306
Row 2	-0.1101	0.1115	0.0651
Row 3	0.7536	-0.0244	-2.9082
Row 4	1.1515	-0.0007	-0.0066
Row 5	0.0180	-0.0463	-0.0123
Row 6	0.6278	-0.1545	-0.2051

b1	Col 1	Col 2	Col 46
Row 1	1.8587	-0.6158	-3.7376

w2	Col 1	Col 2	Col 46
Row 1	-0.0221	0.0263	0.3942
Row 2	0.6408	-0.0455	0.4263
Row 3	0.0025	0.2498	-0.3181
Row 4	-0.0132	-0.1615	2.6238
Row 5	0.0706	0.1371	-2.3721
Row 6	0.0340	-0.0735	-1.4297
Row 7	0.9885	-0.7671	1.6200
Row 8	0.2387	-0.1762	-3.3234
Row 9	0.6095	0.2190	-0.2306
Row 10	-0.0025	-0.1432	1.6481
Row 11	0.0200	0.0131	-1.8189
Row 12	0.3741	-0.1496	0.6168
Row 13	-0.0055	0.1754	-0.1455
Row 14	0.9403	0.3329	0.7198

w3	Col 1
Row 1	1.2533
Row 2	-0.6531
Row 3	0.5335
Row 4	1.9561
Row 5	-0.0338
Row 6	1.6405
Row 7	-0.7694
Row 8	0.1048
Row 9	1.4814
Row 10	0.0376
Row 11	4.3118
Row 12	0.0573
Row 13	1.5323
Row 14	-2.3016

b2	Col 1	Col 2	Col 46
Row 1	1.0587	0.3787	-2.4885

b3	Col 1
Row 1	0.7518

Fig. 6. (a) general NN architecture, (b) NN-based model development, and (c) spreadsheet set-up of the developed M-FS model.

728 (a) (b)

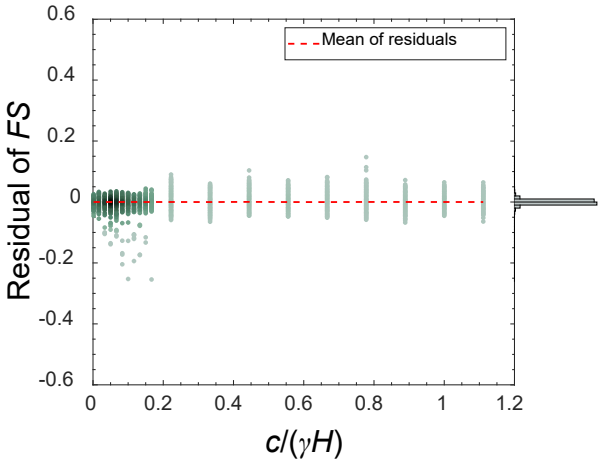

729

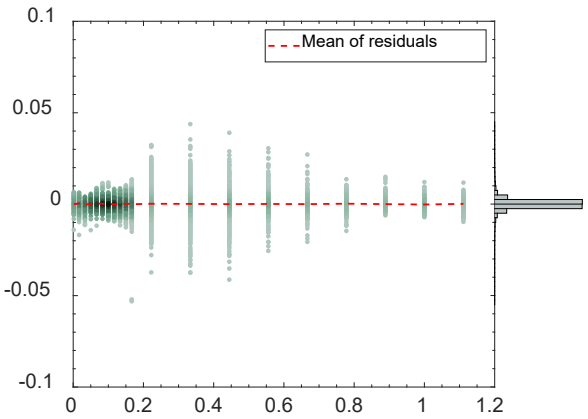

730

731 (c) (d)

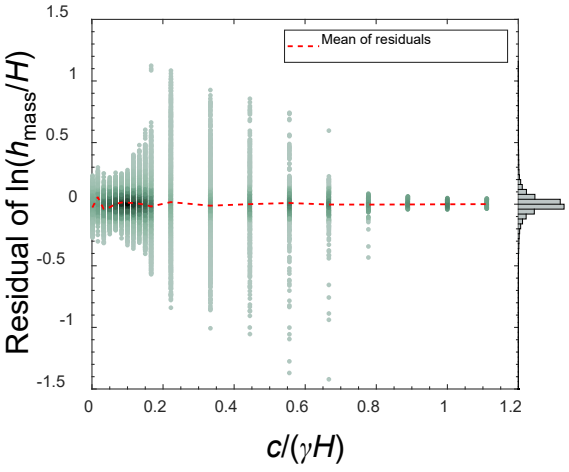

732

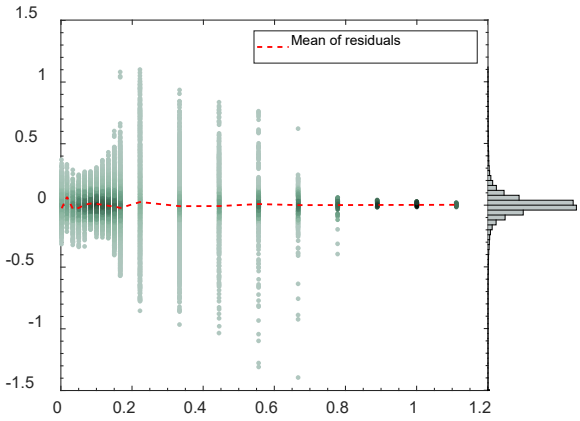

733

734 **Fig. 7.** Distributions of residual versus $c/(\gamma H)$ in predicting (a) FS, (b) k_y, (c) $\ln(h_{mass}/H)$, and (d) $\ln(h_{mass}/h_{tot})$.

735 The scatter grayscale and the histogram on y-axis reflect data density.

736

737 (a) (b)

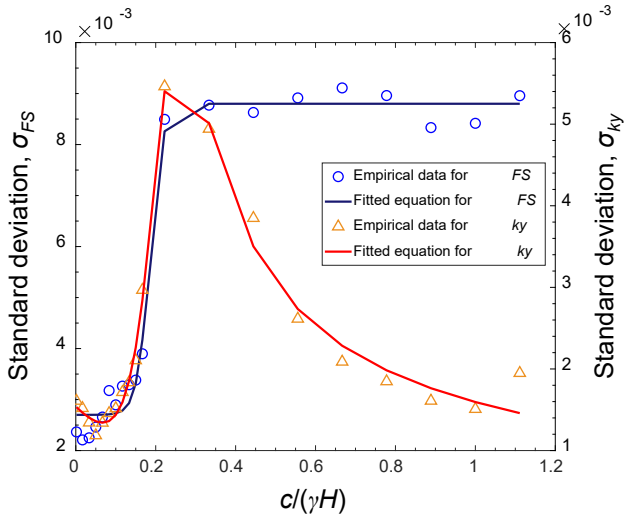

738

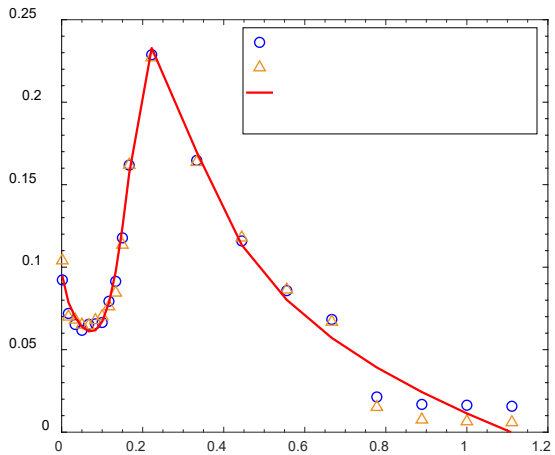

739

740 **Fig. 8.** Standard deviations of residuals for (a) FS and k_y as well as (b) $\ln(h_{mass}/H)$ and $\ln(h_{mass}/h_{tot})$.

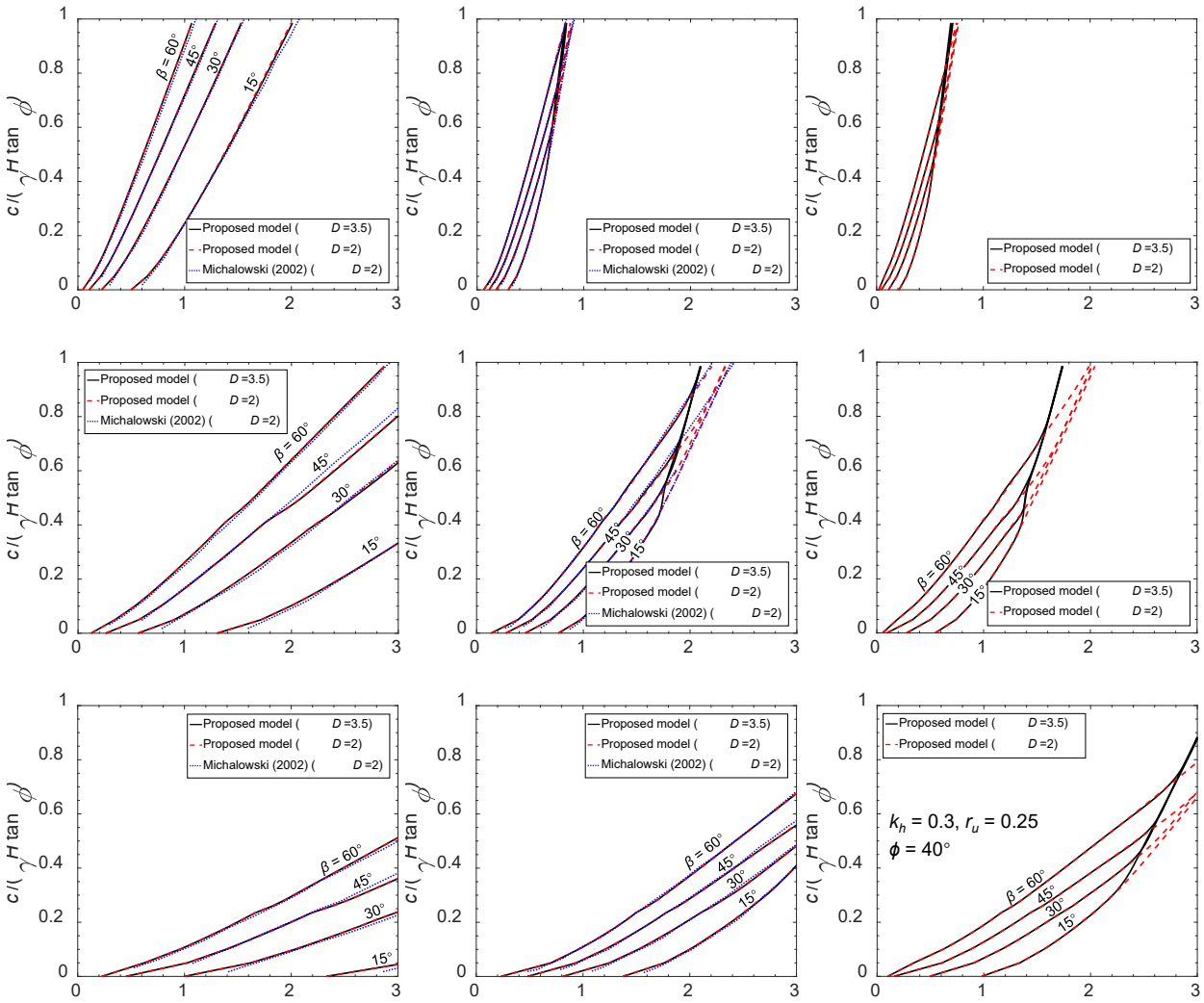

742

743 **Fig. 9.** Distributions of predicted *FS* versus $c/(\gamma H\tan\phi)$ for different values of ϕ, β, D, k_h, and r_u. Also shown

744 are stability chart trends from Michalowski (2002).

745

746

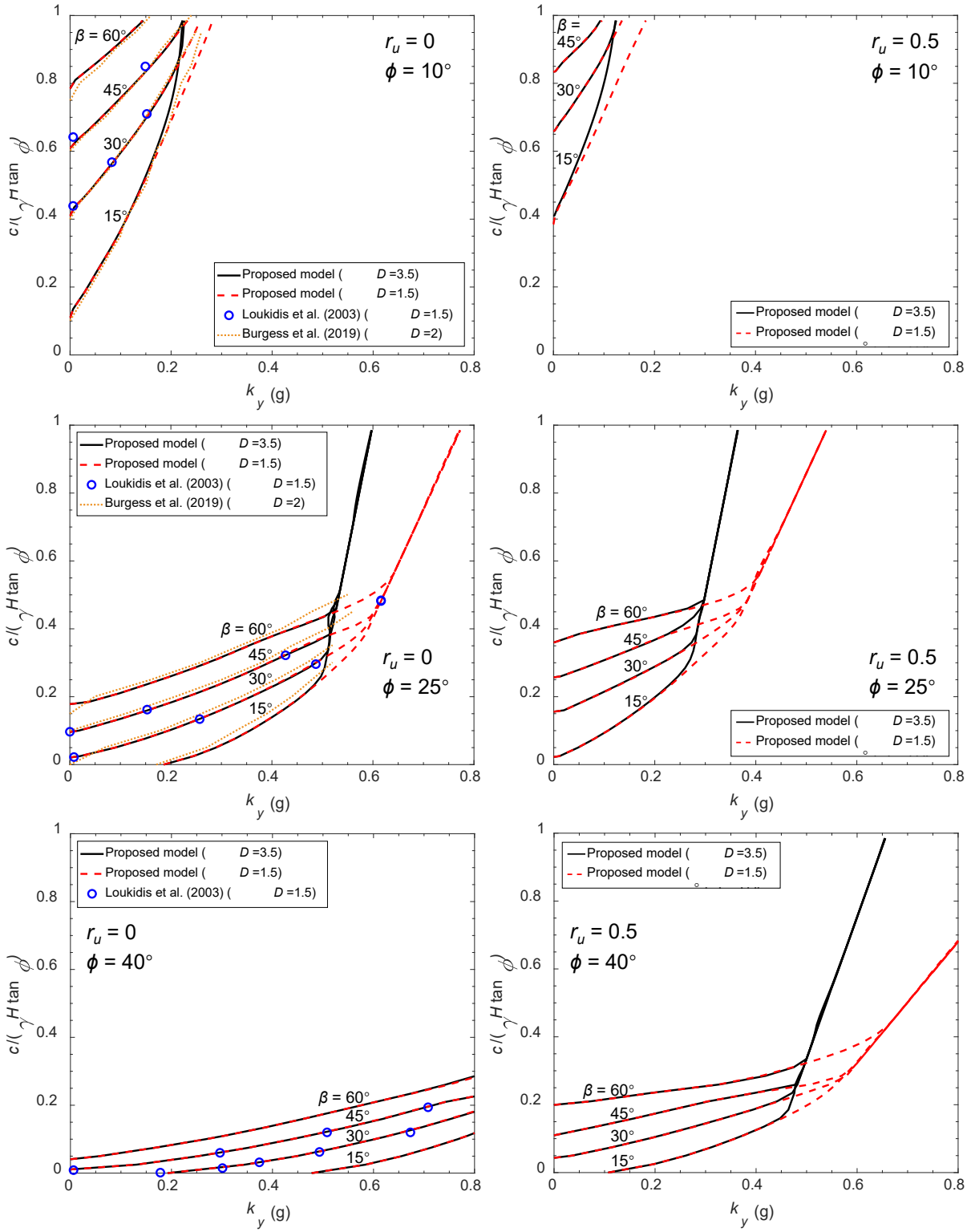

747
748 **Fig. 10.** Distributions of predicted k_y versus $c/(\gamma H \tan\phi)$ for different values of ϕ, β, D, and r_u. Also shown
749 are stability chart trends from Loukidis et al. (2003) and Burgess et al. (2019).

750

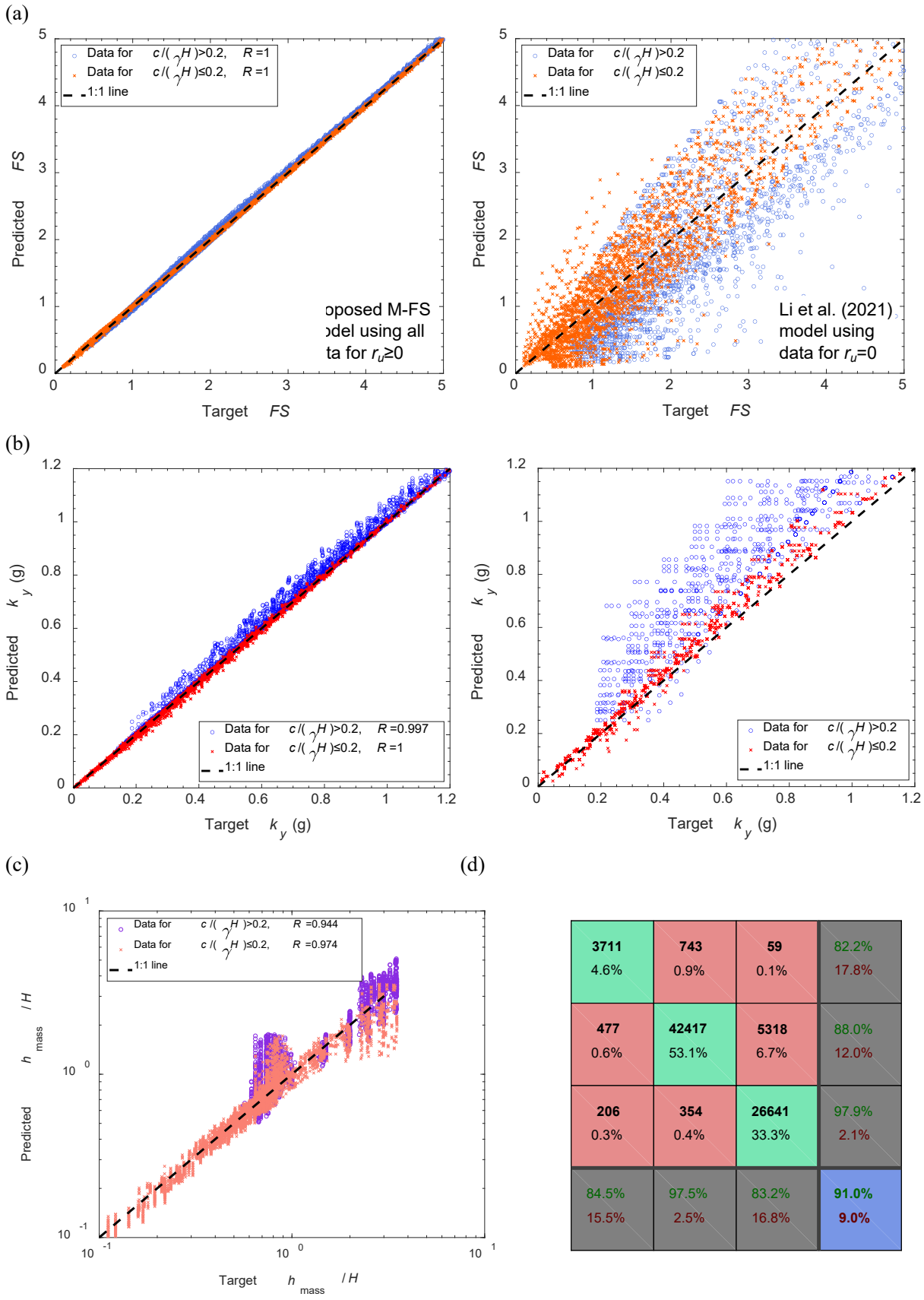

Fig. 11. Blind test results: (a) *FS* predictions from the M-FS model and the Li et al. (2021) model; (b) k_y predictions from the M-KY model and the Chien and Tsai (2017) model; (c) h_{mass}/H prediction from the M-

H model; (d) accuracy rates in failure mode prediction from the M-P model.

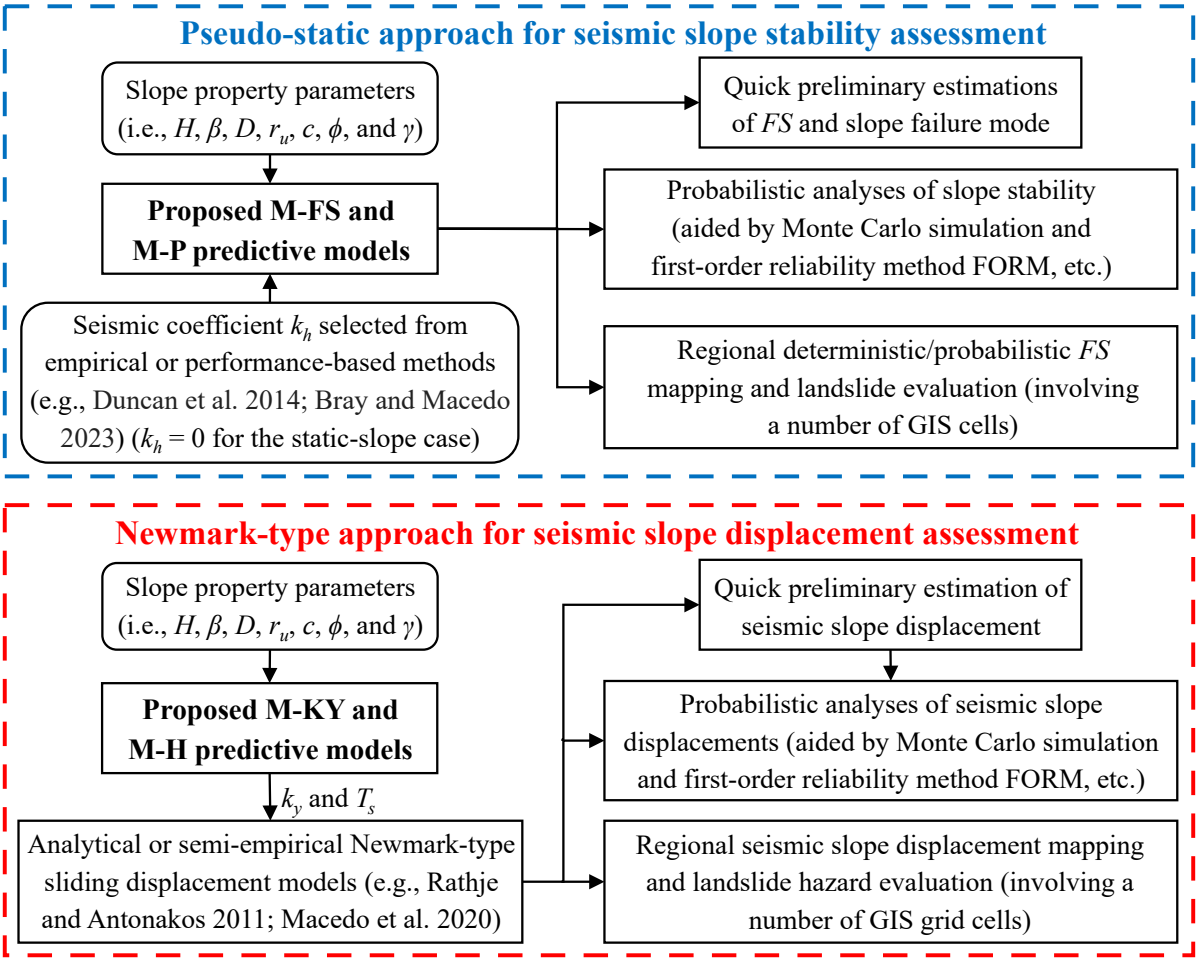

Fig. 12. Potential applications of the models proposed in this study.

762 (a)

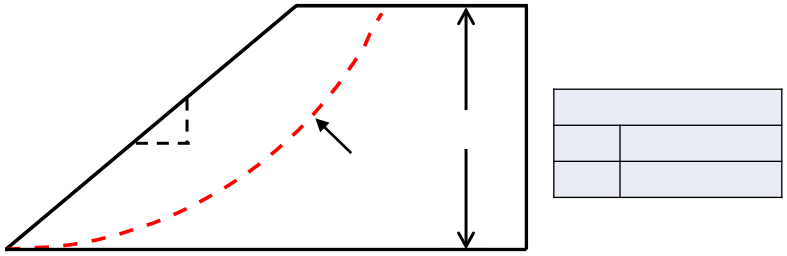

763

764 (b)

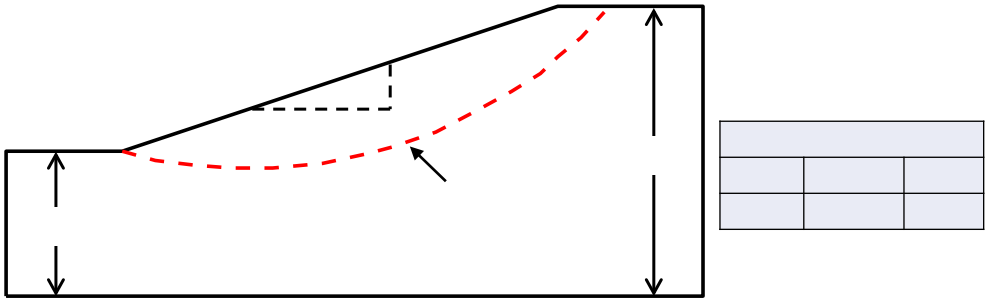

765

766 **Fig. 13.** Slope examples for illustrating the proposed (a) M-FS and M-P models and (b) M-KY and M-H

767 models.

768

769

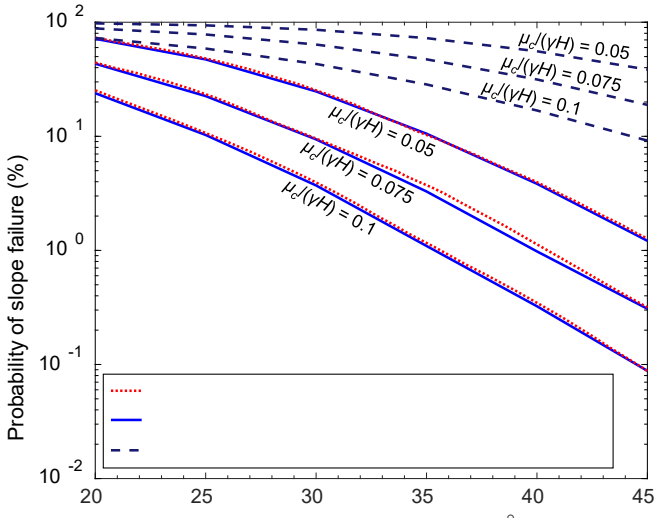

770

771 **Fig. 14.** Capability of the M-FS model for estimating probabilities of both static and seismic slope failures.

772 The other parameters specified are $\beta = 45°$, $COV_c = 0.5$, and $COV_\phi = 0.2$.

773